International Journal of Biological Macromolecules 355 (2026) 151523

Contents lists available at ScienceDirect

International Journal of Biological Macromolecules

journal homepage: www.elsevier.com/locate/ijbiomac

Engineering G-quadruplex aptamer-5-fluoro-2′-deoxyuridine conjugates: Impact of tail orientation and RNA spacer insertion on structure and antitumor activity

Natalia Navarro [a,b,c,1], Daniela Benigno [d,1], Carla Aliberti [d], Antonella Virgilio [d], Aldo Galeone [d], Ramon Eritja [a,b], Veronica Esposito [d,*], Carme Fàbrega [a,b,**]

[a] Nucleic Acids Chemistry Group, Institute for Advanced Chemistry of Catalonia (IQAC-CSIC), Barcelona, 08034, Spain
[b] Nucleic Acids Chemistry Group, Networking Center on Bioengineering, Biomaterials and Nanomedicine (CIBER-BBN), Barcelona, 08034, Spain
[c] University of Barcelona, Barcelona, 08034, Spain
[d] Department of Pharmacy, University of Naples Federico II, Napoli, 80131, Italy

ARTICLE INFO

Keywords:
G-quadruplex aptamer
5-Fluoro-2′-deoxyuridine
Aptamer-drug conjugate
Nucleic acid therapeutics

ABSTRACT

G-quadruplex-forming aptamers represent a promising class of molecules for targeted cancer therapy. However, their therapeutic potential is often limited by a low cytotoxic activity. To overcome this limitation, chemical conjugation with cytotoxic agents has been explored, although rational strategies to optimize such chimeras remain underdeveloped. To enhance the activity of the STAT3-targeting G-quadruplex aptamer (STAT), we covalently attached a 10-mer tail of 5-fluoro-2′-deoxyuridine (FdU) to either its 5′ or 3′ end of the sequence. Structural characterization revealed that the position of the FdU tail modulates the equilibrium between monomeric or dimeric species of STAT aptamer. These structural differences critically impact the chimera's biological properties, including cellular uptake, intracellular trafficking, and *in vitro* cytotoxicity in cancer cells. Moreover, incorporation of an RNA spacer between the aptamer and the FdU tail further increased cytotoxicity by promoting degradation and prodrug activation. Our findings demonstrate that both nature and positional orientation of a chemotherapeutic tail on G-quadruplex aptamers can be strategically employed to modulate both structural conformation and biological function. This work establishes a rational design strategy for engineering aptamer-drug conjugates with tunable structural and cytotoxic properties.

1. Introduction

Nucleic acid aptamers capable of forming G-quadruplex (G4) structures have emerged as a versatile class of therapeutic agents due to their well-defined folding and high affinity for molecular targets [1,2]. G4 aptamers have demonstrated intrinsic antiproliferative effects, particularly in cancer cells, by interacting with proteins such as nucleolin or Signal Transducer and Activator of Transcription 3 (STAT3), which are overexpressed on the surface or within tumor cells [3,4]. Beyond their intrinsic antiproliferative activity, arising from interactions with molecular targets involved in cancer-related pathways [5], G4 aptamers have also been explored for their potential to facilitate cellular uptake or functional engagement in tumor cells [6]. While receptor-mediated targeting has been clearly demonstrated for nucleolin-binding aptamers such as AS1411 [7,8], other G4 structures may exhibit enhanced or preferential internalization in cancer cells without a clearly identified cell-surface receptor [9–13]. This combination of inherent biological activity and context-dependent uptake has motivated the investigation of G4 aptamers as platforms for anticancer applications, including their use as scaffolds for therapeutic cargo delivery [14]. Despite their potential, the clinical application of G4 aptamers remains limited, in part due to modest cytotoxic activity.

To overcome these limitations, various chemical modifications have been explored to enhance aptamer efficacy [15–17]. Among them, the incorporation of cytotoxic moieties, such as small molecules [18,19] or nucleoside analogues [20,21] has shown great potential for combining

* Corresponding author.
** Correspondence to: C. Fàbrega, Nucleic Acids Chemistry Group, Institute for Advanced Chemistry of Catalonia (IQAC-CSIC), Barcelona, 08034, Spain.
E-mail addresses: verespos@unina.it (V. Esposito), carme.fabrega@iqac.csic.es (C. Fàbrega).
[1] Natalia Navarro and Daniela Benigno contributed equally to this work.

https://doi.org/10.1016/j.ijbiomac.2026.151523
Received 17 November 2025; Received in revised form 16 March 2026; Accepted 17 March 2026
Available online 18 March 2026

target specificity with potent biological activity. In particular, the use of antiproliferative nucleoside analogues conjugated or as part of the aptamer itself offers a unique opportunity to construct aptamers with dual function: target recognition and antitumor activity [22].

5-Fluoro-2′-deoxyuridine (FdU), a thymidine analogue, is a well-established anticancer agent that exerts its activity through intracellular conversion into 5-fluoro-2′-deoxyuridine monophosphate (FdUMP). FdUMP irreversibly inhibits thymidylate synthase, a key enzyme in *de novo* DNA synthesis, leading to nucleotide pool imbalance, DNA fragmentation, and ultimately cell death [23,24]. Incorporation of FdU into DNA-based constructs, including oligonucleotides [25,26], and DNA nanostructures [27,28], or in nanoparticles [29] has proven effective in enhancing antiproliferative responses. In this context, a novel polymeric fluoropyrimidine oligonucleotide (ODN), composed of ten serially connected FdU nucleotides, has been developed to act as a nucleic acid prodrug generating active metabolites upon nuclease-mediated degradation and displaying markedly higher cytotoxicity [24].

More recently, a G4-forming aptamer has been successfully employed as a delivery vehicle for FdU, yielding synergistic cytotoxic effects in tumor cells [10]. However, when dealing with G4-based systems, the therapeutic potential of such hybrid constructs cannot be evaluated only on payload incorporation, because G4-forming aptamers are highly sensitive to even small structural perturbations, such as the addition of short nucleotide tails or chemical groups, which can shift the equilibrium between monomeric, dimeric or even higher-order conformations [30]. Consequently, the spatial arrangement of therapeutic units within the nucleic acid scaffold plays a crucial role in the global architecture of the construct and may drastically alter the aptamer's behavior in a cellular environment, including its stability, internalization mechanisms, and intracellular trafficking.

Among G4-forming aptamers, AS1411 is the most extensively studied example and is well known for its antiproliferative activity mediated by interaction with nucleolin [8,31], as well as for its application as a drug carrier in targeted delivery strategies [32–34]. However, a major limitation of AS1411 is the pronounced structural polymorphism it adopts in solution [35], which results in the coexistence of multiple G4 conformations and complicated structure-function correlations. Beyond AS1411, several other G4-forming aptamers have also been reported to display intrinsic antiproliferative effects [1,5,11].

In this context, we chose to focus on the STAT aptamer (T40214), which exhibits promising therapeutic potential due to its ability to inhibit STAT3, a transcription factor that plays a central role in oncogenesis [36,37]. STAT3 is commonly overexpressed and constitutively activated in the cytoplasm and nucleus of tumor cells, as well as in tumor tissue samples, where it regulates the expression of oncogenic genes involved in tumor growth, survival, and metastasis [38–40]. The STAT aptamer, whose sequence is $G_3CG_3CG_3CG_3C$, folds into a well-defined dimeric G4 structure formed by two parallel-stranded G4 units stacked in a 5′-5′ orientation, each characterized by three G-tetrads and three propeller-shaped loops composed of cytidine residues [41,42].

The combination of intrinsic antiproliferative activity, targeting a biologically relevant signaling pathway frequently dysregulated in cancer, and a reproducible G4 architecture with reduced polymorphism represents a significant advantage for mechanistic studies and rational therapeutic design, providing a clear rationale for the choice of the STAT aptamer in the present work.

Herein, we present the design and characterization of a novel series of G4 aptamer-FdU chimeras, in which a 10-mer FdU tail is covalently attached to either the 5′ or 3′ end of STAT aptamer. In parallel, we also generated control constructs carrying a 10-mer thymidine sequence at the 5′ or 3′ end of the same aptamer, serving as reference oligomers devoid of chemotherapeutic nucleosides but maintaining comparable structural extension. Through biophysical and cellular assays, we study the role of the positioning of the FdU tail in the oligomeric state and in *in vitro* activity. Furthermore, the insertion of an RNA spacer between the aptamer core and the FdU tail was evaluated as a strategy to enhance intracellular degradation and prodrug activation, thereby improving the overall cytotoxic response. In this context, a direct comparison with an analogous construct incorporating a DNA linker was also performed to assess the impact of linker chemistry on stability and biological performance. The constructs described above are reported in Table 1, while a comprehensive overview of all oligonucleotides and their corresponding properties is provided in Table S1.

Together, these findings establish a comprehensive structure-activity relationship and introduce a rational design strategy to modulate the therapeutic performance of aptamer-drug conjugates through positional control of chemotherapeutic nucleoside tails and RNA spacer engineering.

2. Material and methods

2.1. Materials and instrumentation

Phosphoramidites, auxiliary reagents, and solvents for oligonucleotide synthesis were purchased from Applied Biosystems (USA) and LGC Biosearch Technologies (UK). Standard automated solid-phase DNA synthesis was performed on a K&A H16-SE and K&A H8-SE solid-phase DNA-synthesizers (K&A Laboratories, Germany). Oligonucleotide purification cartridges (OPC) were purchased from Glen Research (NAP-10 column (GE Healthcare, UK)). Hellma® cuvettes made of quartz glass were purchased from Hellma Analytics (Sigma-Aldrich, USA). HCC2998 were kindly provided by Dr. Diego Arango (Vall d'Hebron), and MDA-MB-231 (HTB-26) and Fibroblasts (PCS-201-012) were purchased from ATCC (LGC, Spain). Dulbecco's modified Eagle's medium (DMEM) and fetal bovine serum (FBS) were purchased from Thermo Fisher Scientific Inc. (USA). All other common chemical reagents were purchased from Sigma-Aldrich (Spain).

Mass spectra were recorded on a MALDI Voyager DE RP time-of-flight (TOF) spectrometer (Applied Biosystems, USA) equipped with a nitrogen laser at 337 nm using a 3 ns pulse. Oligonucleotide identity was confirmed by high-performance liquid chromatography (HPLC) using an LC-4000 Series HPLC system (Jasco, Tokyo, Japan) equipped with a Nucleogel SAX column (1000–8/46, Macherey-Nagel, Germany). All circular dichroism (CD) experiments were recorded on a Jasco 715 CD spectrophotometer equipped with a PTC-348 temperature-controlled cell holder (Jasco, Tokyo, Japan). UV experiments were recorded on a Jasco V 750 UV/Vis spectrophotometer (Jasco, Tokyo, Japan). Fluorescence emission spectra were recorded using a Jasco FP-8350 spectrofluorometer (Jasco, Tokyo, Japan). Electrophoresis was carried out using a VWR® PerfectBlue Twin M Dual-Gel System (VWR/Avantor, Germany). The flow cytometer was a Guava easyCyte (GuavaSoft, Millipore, USA), and data were analyzed using InCyte v.3.2 (GuavaSoft, Millipore, USA). Confocal images were acquired with a Carl Zeiss LSM880 (Zeiss, Germany). Absorbance values of 1-(4,5-dimethylthiazol-2-yl)-3,5-diphenylformazan (MTT) assays were measured in an automated spectrophotometric plate reader Glomax multi detection system (Promega, USA).

Table 1
Names and sequences of the representative constructs investigated in this study.

Name	Sequence (5′–3′)
STAT	GGGCGGGCGGGCGGGC
STAT-FdU_{10}	GGGCGGGCGGGCGGGC$(FdU)_{10}$
FdU_{10}-STAT	$(FdU)_{10}$GGGCGGGCGGGCGGGC
STAT-T_{10}	GGGCGGGCGGGCGGGC$(T)_{10}$
T_{10}-STAT	$(T)_{10}$GGGCGGGCGGGCGGGC
STAT-U-FdU_{10}	GGGCGGGCGGGCGGGCTTUUUTT$(FdU)_{10}$
STAT-T-FdU_{10}	GGGCGGGCGGGCGGGCTTTTTTT$(FdU)_{10}$

2.2. Methods

2.2.1. Oligonucleotide synthesis and analysis

Oligonucleotides were synthesized on K&A H-16 and H-8 DNA synthesizers (K&A Laboratories, Germany) at the 1 μmol scale (control pore glass (CPG) synthesis) using standard protocols. The resulting oligonucleotides were deprotected by treatment with concentrated aqueous ammonia (32%) overnight r.t., followed by 1 h at 55 °C, and then desalted using a NAP-10 column (GE Healthcare, UK). The STAT-U-FdU_{10} oligonucleotide was synthesized in DMT-ON mode by conventional solid-phase RNA phosphoramidite chemistry, using 2'-O-TBDMS-protected ribonucleoside phosphoramidites, following standard coupling, capping, oxidation, and deprotection steps [43]. After cleavage from the solid support under standard conditions, the 2'-O-TBDMS protecting groups were removed by treatment with 37% triethylamine trihydrofluoride at 45 °C for 2 h. The crude oligonucleotide was then purified using an OPC Cartridge (Glen Research, UK) following the manufacturer's standard protocol. Oligonucleotide identity was confirmed by HPLC on a Nucleogel SAX column (1000–8/46, Macherey-Nagel, Germany) using buffer A (20 mM NaH_2PO_4/Na_2HPO_4 aqueous solution (pH 7.0) containing 20% (v/v) CH_3CN) and buffer B (1 M NaCl, 20 mM NaH_2PO_4/Na_2HPO_4 aqueous solution (pH 7.0) containing 20% (v/v) CH_3CN); a linear gradient from 0% to 100% B for 60 min and a flow rate of 1 mL/min were used (Fig. S1). The expected mass was confirmed by MALDI-TOF (Table S1 and Fig. S2). The matrix used contained 2,4,6-trihydroxyacetophenone (THAP, 10 mg/mL in ACN/water 1:1) and ammonium citrate (50 mg/mL in water).

2.2.2. Circular dichroism spectroscopy

CD samples were prepared at a concentration of 25 μM using a potassium phosphate buffer (5 mM KH_2PO_4/K_2HPO_4, 5 mM KCl, pH 7.0) and submitted to the annealing procedure by heating at 90 °C, followed by slow cooling to room temperature over 12 h. STAT was also prepared in 10 mM lithium cacodylate buffer (pH 7.2) and subsequently subjected to the annealing procedure, as reported above. The CD spectra were recorded at 20 °C over a 220–320 nm wavelength range with a scanning speed of 100 nm/min, a response time of 4 s, a 0.1 nm data pitch, and normalized by subtraction of the background scan with the potassium buffer. CD melting curves were recorded as a function of temperature (20–95 °C) by monitoring the CD signal at a single fixed wavelength corresponding to the maximum Cotton effect for each G4. The data were recorded in a 0.1 cm pathlength cuvette (Sigma-Aldrich, USA) with a scan rate of 0.5 °C/min. All CD experiments were recorded on a Jasco 715 CD spectrophotometer (Jasco, Tokyo, Japan) equipped with a PTC-348 temperature-controlled cell holder (Jasco, Tokyo, Japan).

2.2.3. UV thermal difference spectra (TDS)

UV samples (2 μM) of investigated oligonucleotides were prepared using a potassium phosphate buffer (5 mM KH_2PO_4/K_2HPO_4, 5 mM KCl, pH 7.0). For each oligonucleotide sample, a UV spectrum was recorded above and below its melting temperature (T_m). All experiments were conducted on a Jasco V 750 UV/Vis spectrophotometer (Jasco, Tokyo, Japan) using quartz cuvettes (Sigma-Aldrich, USA) with an optical path of 1 cm. Absorbance spectra were recorded in the 220–340 nm range, with a scan speed of 200 nm/min and with a data interval of 1 nm. The difference between the UV spectra at high (95 °C) and low (20 °C) temperatures was defined as the TDS, which represents the spectral difference between the unfolded and folded forms. The temperature (20 or 95 °C) was kept constant with a thermostatic circulating water bath for cell holders (Jasco CTU-100). The thermal difference spectra were normalized, setting the highest positive peak to +1.

2.2.4. Fluorescence emission spectra

Samples were prepared at a concentration of 2 μM using a potassium phosphate buffer (5 mM KH_2PO_4/K_2HPO_4, 5 mM KCl, pH 7.0) and annealed as previously reported. STAT was also prepared in 10 mM lithium cacodylate buffer (pH 7.2) and subsequently subjected to the annealing procedure, as reported above. Fluorescence emission spectra were recorded with a Jasco FP8350 spectrofluorometer (Jasco, Tokyo, Japan). For each sample, the spectrum was acquired using $\lambda_{ex} = 260$ nm and an emission range of 300–500 nm (slit widths: 5 nm for both excitation and emission beams) in a quartz cuvette (1 cm path length) (Sigma-Aldrich, USA). For the spectra data pitch was fixed to 1 nm and the integration time to 1 s. All spectra were corrected with a blank spectrum of the appropriate buffer solution.

2.2.5. Polyacrylamide gel electrophoresis (PAGE)

All oligonucleotides were analyzed by PAGE under native conditions. All oligonucleotide samples were initially prepared at a concentration of 500 μM in potassium phosphate buffer and underwent the annealing procedure as described previously. Subsequently, 1 μL of the annealed solution was mixed with glycerol/TBE 10× loading solution, resulting in a final oligonucleotide concentration of 50 μM prior to gel loading. Each sample was loaded onto a 20% polyacrylamide gel containing TBE 2.5× and 5 mM KCl. The running buffer was TBE 1× supplemented with 20 mM KCl. Electrophoresis was carried out at 10 V/cm for at least 2 h at 20 °C. Subsequently, bands were visualized by UV shadowing.

2.2.6. Cell culture

HCC2998 (colorectal cancer cells), MDA-MB-231 (breast cancer cells), and PCS-201-012 (human dermal fibroblast cells) were maintained in DMEM supplemented with 10% FBS at 37 °C in 5% CO_2. Cells were passed every 3 days at a ratio of 1:5 and routinely tested for mycoplasma. Cultures were maintained for 3–4 passages after thawing prior to all *in vitro* experiments.

2.2.7. Cellular uptake

To assess cellular internalization by flow cytometry of FAM-labeled constructs, cells were seeded at a density of 80,000 *cells per well* in 24-well plates. The next day, FAM-labeled oligonucleotides, previously annealed in potassium-containing buffer as reported before, were dissolved in fresh medium to a final concentration of 1 μM. The samples were incubated for 2, 4, 6, and 24 h. Cells were then washed twice with PBS and trypsinized for 15 min to avoid unspecific signals from any compounds still attached to the membranes. After harvesting, the cells were resuspended in cell culture medium and centrifuged at 1000 rpm for 8 min. This process was repeated twice and the remaining cell pellet was resuspended in cold PBS. Each condition was assayed in duplicate.

2.2.8. Retention experiment

Retention experiments were conducted following the same procedure described in the *Cellular uptake* subsection, with the only modification that, 24 h after sample incubation, cells were washed with PBS and the medium was replaced. Subsequently, cells were collected at 24 h (i.e., 48 h after sample addition) and 48 h (i.e., 72 h after initial exposure). Each condition was assessed in duplicate.

2.2.9. Confocal microscopy

For live-cell imaging, MDA-MB-231 cells were seeded at a density of 500,000 *cells per 35 mm* MatTek Petri dish (MatTek Corporation, USA). After 24 h, cells were incubated with 1 μM of compounds in 750 μL of phenol red-free DMEM for 6 h. Cells were washed with PBS and stained with Hoechst 33342 (Thermo Fisher Scientific, USA, 0.2 μg/mL) for nuclear staining and WGA55 (Thermo Fisher Scientific, USA, 0.1 μg/mL) for membrane staining for 15 min in the dark. Confocal fluorescence images were acquired using a Carl Zeiss LSM880 microscope equipped with a Plan-Apochromat 63×/1.4 oil immersion objective. Image analysis was performed using FIJI software (v2.16.0).

2.2.10. Cellular viability assay

The cytotoxicity of the oligonucleotides was evaluated using the 1-

(4,5-dimethylthiazol-2-yl)-3,5-diphenylformazan (MTT) assay. The day before, cells were seeded at a density of 5000 *cells per well* in 96-well plates and cultured overnight. Subsequently, pre-annealed samples at different concentrations (0.5 μM, 1 μM, 5 μM, 10 μM, and 20 μM) were added. After 48 h, 72 h, and 96 h the cells were washed with PBS and MTT reagent was added to each well, resulting in a final concentration of 0.5 mg/mL. After 2 h of incubation, the medium was carefully removed and formazan crystals were dissolved by adding DMSO. The absorbance values were measured at 570 nm. This assay was repeated three independent times in triplicate. Data were normalized to the value of untreated cells (100% viability).

2.2.11. Apoptosis

Apoptotic cells induced by treatment with the different compounds were detected using flow cytometry with fluorescein isothiocyanate (FITC)-conjugated Annexin V and propidium iodide (PI). HCC2998 and MDA-MB-231 cells were seeded in 24-well plates at a density of 50,000 *cells per well*. After a 24 h incubation, cells were exposed to the test compounds at 1 μM in a final volume of 500 μL for 6 h. After 72 h, both adherent and non-adherent cells were harvested, washed twice with cold PBS, and resuspended in 100 μL of Annexin binding buffer containing FITC-Annexin V and PI (BioLegend, USA), following the manufacturer's instructions. Two independent experiments were conducted, each in duplicate.

2.2.12. Nuclease degradation assay

Nuclease stability assay of modified oligonucleotides was conducted in a 10% FBS solution diluted with DMEM at 37 °C. Prior to serum incubation, the oligonucleotides were annealed in the same potassium-containing buffer used for all biophysical experiments to ensure proper G-quadruplex folding. Following annealing, the pre-folded oligonucleotides were incubated in the serum-containing medium at a final concentration of 10 μM. Aliquots (50 μL) were collected at different times and analyzed by HPLC, performed on a Nucleogel SAX column (Macherey-Nagel, Düren, Germany, 1000–8/46) with buffer A (20 mM NaH_2PO_4/Na_2HPO_4, pH 7.0, 20% (v/v) CH_3CN) and buffer B (1 M NaCl in 20 mM phosphate buffer, 20% (v/v) CH_3CN) using a linear gradient 0–100% B over 60 min at 1 mL/min. Peak areas were baseline-corrected by subtraction of medium blank, and degradation was calculated as the reduction in peak area over time. In parallel, the nuclease stability of STAT-U-FdU_{10} and STAT-T-FdU_{10} was also evaluated by native PAGE. For this analysis, both ODNs were evaporated to dryness under reduced pressure and incubated with 300 μL of 10% FBS at 37 °C. Aliquots (50 μL) were collected and stored at −20 °C for at least 20 min. Samples were then dried, resuspended in 5 μL of gel loading buffer (glycerol/TBE 10×), and analyzed by PAGE using a 20% polyacrylamide gel in 1× TBE buffer at room temperature. Bands were visualized by UV shadowing.

2.2.13. Statistical analysis

Statistical analysis was performed using GraphPad Prism 8 (GraphPad Software, Inc., La Jolla, CA, USA). Quantified data are expressed as mean ± standard deviation (SD). Two-way ANOVA with Tukey post hoc test was used to evaluate statistical differences, with significance levels indicated as follows: (*$p \leq 0.0332$, **$p \leq 0.0021$, ***$p \leq 0.0002$, **** $p \leq 0.0001$).

3. Results and discussion

3.1. Structural insight

To elucidate the structural features of the designed G4 derivatives (Fig. 1 and Tables 1 and S1) and to evaluate the effect of tail conjugation on their folding topology and supramolecular organization, a biophysical characterization was carried out. In particular, we aimed to determine whether the attachment of thymidine or FdU stretches at the 5′ or 3′ termini could modulate the monomer-dimer equilibrium and influence the overall structural stability of the G4 scaffold.

CD and UV spectroscopy, intrinsic fluorescence and non-denaturing

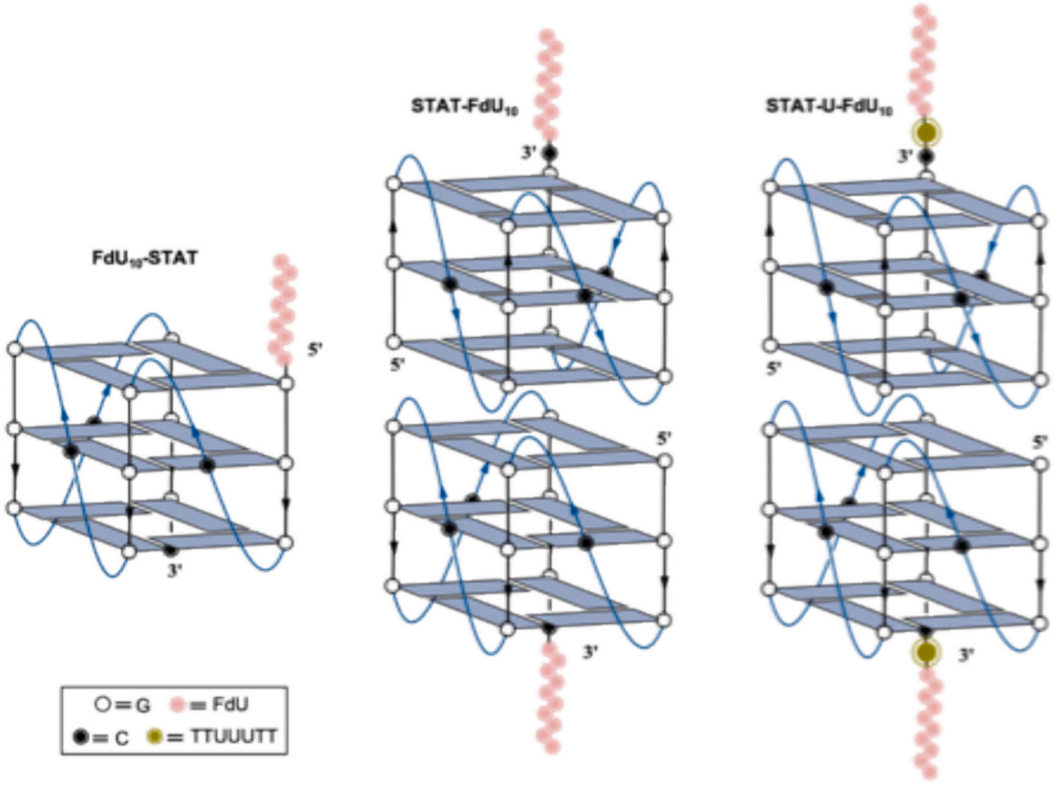

Fig. 1. Schematic representation of the G4 structures adopted by the conjugated sequences studied.

PAGE were employed as complementary techniques to monitor conformational integrity and to gain insights into the molecular organization of the different constructs.

All derivatives showed CD signatures highly consistent with the parent aptamer (Fig. 2). In each case, spectra were characterized by a negative band at 242 nm and a positive one at 263 nm, confirming a parallel topology in which all guanosines adopt *anti*-glycosidic conformations. The preservation of these characteristic features across all variants indicates that the introduction of the thymidine or FdU tails did not perturb the parallel folding of the G4 core. To further support this conclusion, CD spectra of the isolated T_{10} and FdU_{10} sequences are provided in Fig. S3. Both oligonucleotides display essentially featureless CD profiles, confirming that the observed CD signal originates exclusively from the STAT G4-scaffold.

CD melting experiments were therefore conducted to assess the impact of tail position on the thermal stability of the G4 structures (Fig. S4). To better reveal possible subtle differences in G4 structures' stability, these experiments were performed under conditions that do not overly stabilize them (5 mM KH_2PO_4/K_2HPO_4, 5 mM KCl, pH 7.0). The results demonstrated that the conjugation does not significantly compromise the structural integrity of the G4 framework. Indeed, in this low-potassium environment, all constructs showed modest reductions in melting temperature compared to the parent STAT sequence, yet the decrease was limited and did not reflect any major destabilization of the G4 architecture (Table S1).

To support the CD spectroscopy data, UV spectroscopic analyses were performed using thermal difference spectra (TDS) (Fig. 3). This technique allows comparison between the unfolded and folded states of the oligonucleotides induced by thermal denaturation and is particularly sensitive to base-stacking interactions. All analyzed sequences exhibited highly similar TDS profiles, characterized by two positive bands in the 240–275 nm region and a pronounced negative band centered at approximately 295 nm [35,44]. This spectral signature is widely recognized as the fingerprint of G-quadruplex structures. The close overlap of the TDS profiles among all conjugates indicates that, despite the introduction of tails, all sequences adopt comparable G4 conformations. These results are in full agreement with the CD results and further support the formation of G4 structures. In order to confirm STAT G4 folding, CD and intrinsic fluorescence spectra recorded under stabilizing (K^+-containing buffer) and non-stabilizing (Li^+-containing buffer) conditions were compared (Fig. S5), showing the expected loss of G4 signal in the presence of lithium.

Overall, these data indicate that the core G4 structure is preserved regardless of the tail position and composition, thus suggesting that the appended sequences may mainly influence the equilibrium between monomeric and dimeric assemblies rather than the intrinsic stability of individual G4 units. Indeed, to explore the effect of tail positioning on the supramolecular organization, the intrinsic fluorescence of the designed conjugates was investigated. Upon excitation at 260 nm, distinct emission profiles were observed reflecting the oligomeric state

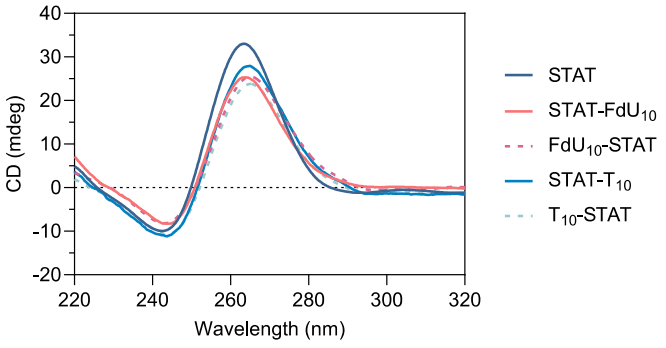

Fig. 2. CD spectra at 20 °C of the investigated ODNs in a potassium phosphate buffer (5 mM KH_2PO_4/K_2HPO_4, 5 mM KCl, pH 7.0).

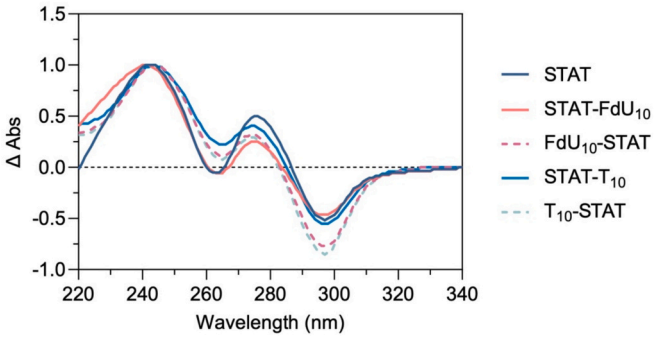

Fig. 3. Normalized TDS profiles of the investigated ODNs in a potassium phosphate buffer (5 mM KH_2PO_4/K_2HPO_4, 5 mM KCl, pH 7.0).

of the structures (Fig. 4). STAT aptamer and constructs bearing thymidine or FdU stretches at the 3′ end exhibited markedly higher fluorescence intensity, characterized by an intense redshifted band at 385 nm, indicative of strong π–π interactions between guanine six-membered rings at 5′-5′ stacking interfaces and consistent with the formation of dimeric assemblies [45,46]. In contrast, G4 constructs T_{10}-STAT and FdU_{10}-STAT, with the tail at the 5′ end, display weaker emission dominated by a band around 330 nm, typical of parallel monomeric G4 containing only three stacked tetrads [45,47].

Further insights into the supramolecular organization were obtained through native PAGE, performed under non-denaturing conditions (Fig. 5). When interpreting the PAGE migration patterns of the different constructs, both the total number of nucleobases and the molecularity of the G4 assemblies must be considered. The parent dimeric aptamer STAT (16mer, lane 3) and its monomeric control, TT-STAT (18mer, lane 6), were loaded in gel as references [48]. The expected difference in supramolecular organization was confirmed by TT-STAT migrating significantly faster than STAT. The remaining constructs all contain 26 nucleobases, i.e., ten additional bases relative to STAT, but distinct migration behaviors were observed depending on the position of the appended tails. Constructs carrying the FdU or thymidine stretches at the 3′ end, STAT-FdU_{10} (26mer, lane 4) and STAT-T_{10} (26mer, lane 5), showed a pronounced retardation in gel mobility compared to STAT dimer, consistent with an increased size associated with dimer formation, plus the addition of the tails that further slowed down the migration. Conversely, sequences functionalized at the 5′ end, T_{10}-STAT (26mer, lane 1) and FdU_{10}-STAT (26mer, lane 2), migrated faster than their 3′-modified dimeric counterparts, yet slower than the monomeric TT-STAT, consistent with the presence of the tail. This behavior unambiguously confirms their monomeric nature.

Collectively, these findings provide a comprehensive picture of the structural organization of the G4 conjugates. While CD confirmed the preservation of a parallel folding topology across all constructs, intrinsic fluorescence and PAGE revealed that the position of the appended tails modulates the supramolecular behavior, either preserving the native 5′-5′ dimeric arrangement characteristic of the original aptamer or hindering this interaction, thereby leading to a prevalent formation of monomeric G4 species.

Furthermore, the insertion of an RNA spacer, together with its corresponding DNA analogue, between the aptamer core and the FdU tail was evaluated to assess the impact of linkers on folding, stability, and molecularity of the STAT-FdU_{10} conjugate (Fig. 6). To this end, a mixed linker with the sequence 5′-TTUUUTT-3′, in which the central uridines introduce an RNA segment and the flanking thymidines act as flexible DNA spacers, was inserted to generate STAT-U-FdU_{10}. In parallel, a fully DNA-linker-based analogue (STAT-T-FdU_{10}) was synthesized as a reference. CD spectroscopy revealed that both constructs display the characteristic spectral signature of a parallel G4 with all Gs adopting an *anti*-glycosidic conformation (Fig. 6a and e), while CD melting experiments confirmed that the introduction of either RNA or DNA spacer does

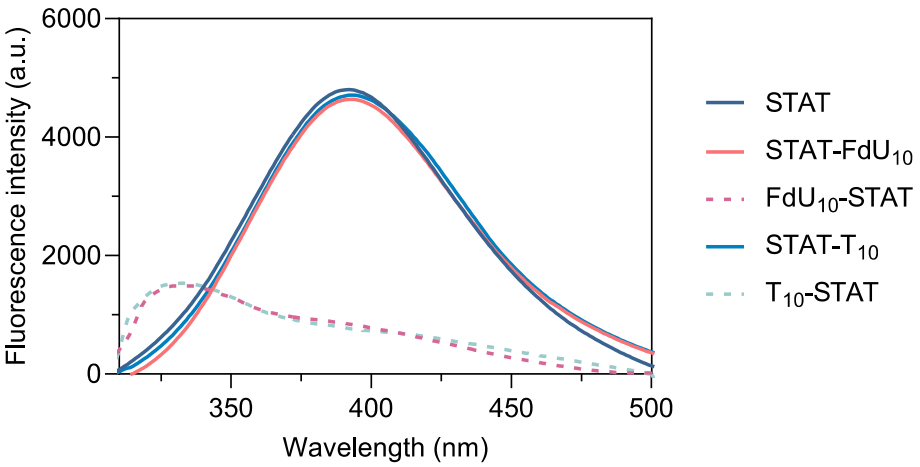

Fig. 4. Fluorescence emission spectra of the investigated ODNs in potassium phosphate buffer (5 mM KH_2PO_4/K_2HPO_4, 5 mM KCl, pH 7.0) under 260 nm excitation.

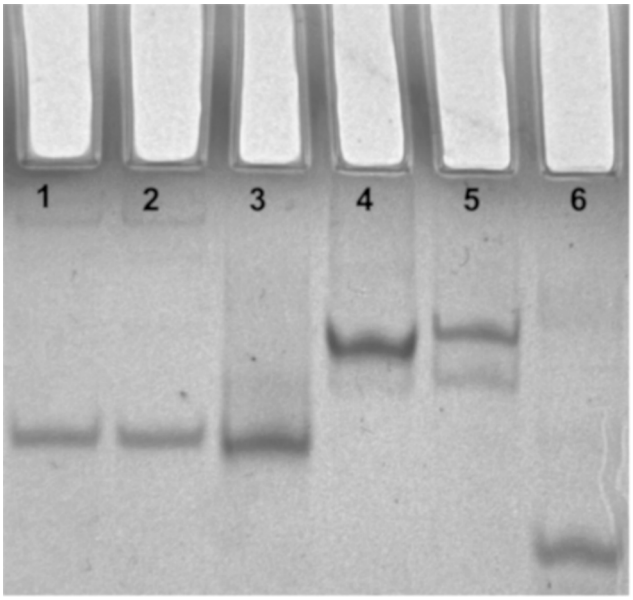

Fig. 5. PAGE analysis of the studied ODNs. Lane 1: T_{10}-STAT; lane 2: FdU_{10}-STAT; lane 3: STAT; lane 4: STAT-FdU_{10}; lane 5: STAT-T_{10}; lane 6: TT-STAT.

not compromise the thermal stability of the G4 architecture (Table S1, Fig. 6b and f). Consistently, thermal difference spectra (TDS) showed the canonical G4 fingerprint, further corroborating the preservation of G4 folding upon linker insertion (Fig. 6c and g).

Fluorescence measurements indicate the prevalence of a dimeric species, in line with what is observed for the parental STAT and STAT-FdU_{10}/T_{10} systems (Fig. 6d and h). The molecularity of the constructs was further confirmed by native PAGE analysis, which showed that both linker-containing constructs migrate more slowly than the two dimeric references STAT and STAT-FdU_{10}, consistent with a dimeric organization (Fig. 6i). Overall, these combined biophysical analyses demonstrate that the incorporation of either an RNA or a DNA linker between the STAT aptamer core and the FdU tail preserves the native G4 topology and dimeric behavior of the parental construct, thereby providing a robust structural framework for subsequent evaluation of their biological performance.

3.2. Time-dependent cellular internalization

For cellular studies, HCC2998 colorectal cancer cells and MDA-MB-231 breast cancer cells were used as tumor cell lines. Human dermal fibroblasts (PCS-201-012) were employed as a non-cancer control cell line to compare cellular responses between malignant and normal cells. Efficient cellular uptake is a critical parameter for aptamer-drug conjugates, particularly when the therapeutic component requires metabolic activation within the cell. To evaluate the impact of the position of the FdU tail on uptake kinetics of the STAT G4 aptamer, we examined time-dependent internalization of the two variants of STAT-FdU constructs at 2, 4, 6, and 24 h (Figs. 7 and S6). ODNs were labeled with fluorescein (FAM) either at the 3′ or 5′-position (Table S1) to allow for tracking of cellular internalization. Notably, FAM labeling does not alter G-quadruplex folding, as confirmed by the preservation of the characteristic CD spectral signature and CD melting (Fig. S7a and b), nor does it affect the molecularity of the conjugates. Indeed, consistent with the behavior observed for the corresponding unlabeled sequences, 5′-end FAM labeling yields predominantly monomeric species (FAM-FdU_{10}-STAT), whereas 3′-end labeling favors dimer formation (STAT-FdU_{10}-FAM), as demonstrated by native PAGE analysis (Fig. S7c). Flow cytometry analysis in HCC2998 and MDA-MB-231 (Fig. 7 and Table S2) revealed that the 3′ end FdU_{10}-modified aptamer consistently exhibited faster and higher cellular uptake than its monomeric 5′ end modified FdU_{10} counterpart in both HCC2998 and MDA-MB-231 cells. Dimeric nucleic acid structures are known to facilitate receptor clustering and enhance avidity-driven endocytosis [10,48–51]. In this case, the dimeric conformation may promote the engagement with overexpressed cancer cell receptors, leading to more efficient receptor-mediated internalization.

To further study in detail the determinants of uptake, we included control aptamers lacking the FdU_{10} tail and labeled with FAM at either the 5′ or 3′ end (FAM-STAT and STAT-FAM) (Table S1). Also, in this case, CD spectroscopy confirmed the preservation of the G4 folding (Fig. S7a and b), while native PAGE analysis revealed a molecularity dependent on the position of the fluorophore: 5′-end labeling resulted in monomeric species, whereas 3′-end labeling favored dimer formation (Fig. S7c). Linear oligonucleotides (T_{10} and FdU_{10}) were also tested as additional controls (Table S1). These controls allowed us to attribute the observed differences in internalization profiles not only to the dimer's architecture but also to the presence of fluorinated residues, in good consistency with previous works reporting similar trends [10,26]. In addition, FdU_{10} showed enhanced uptake in MDA-MB-231 cells compared to HCC2998. Notably, when comparing both dimeric constructs, namely STAT-FAM and STAT-FdU_{10}-FAM, the latter reached a plateau from 4 h to 24 h. This suggests that the FdU_{10} tail may also accelerate internalization kinetics while there is a direct relationship between structural conformation and intracellular delivery, with dimerization conferring clear advantages in uptake dynamics.

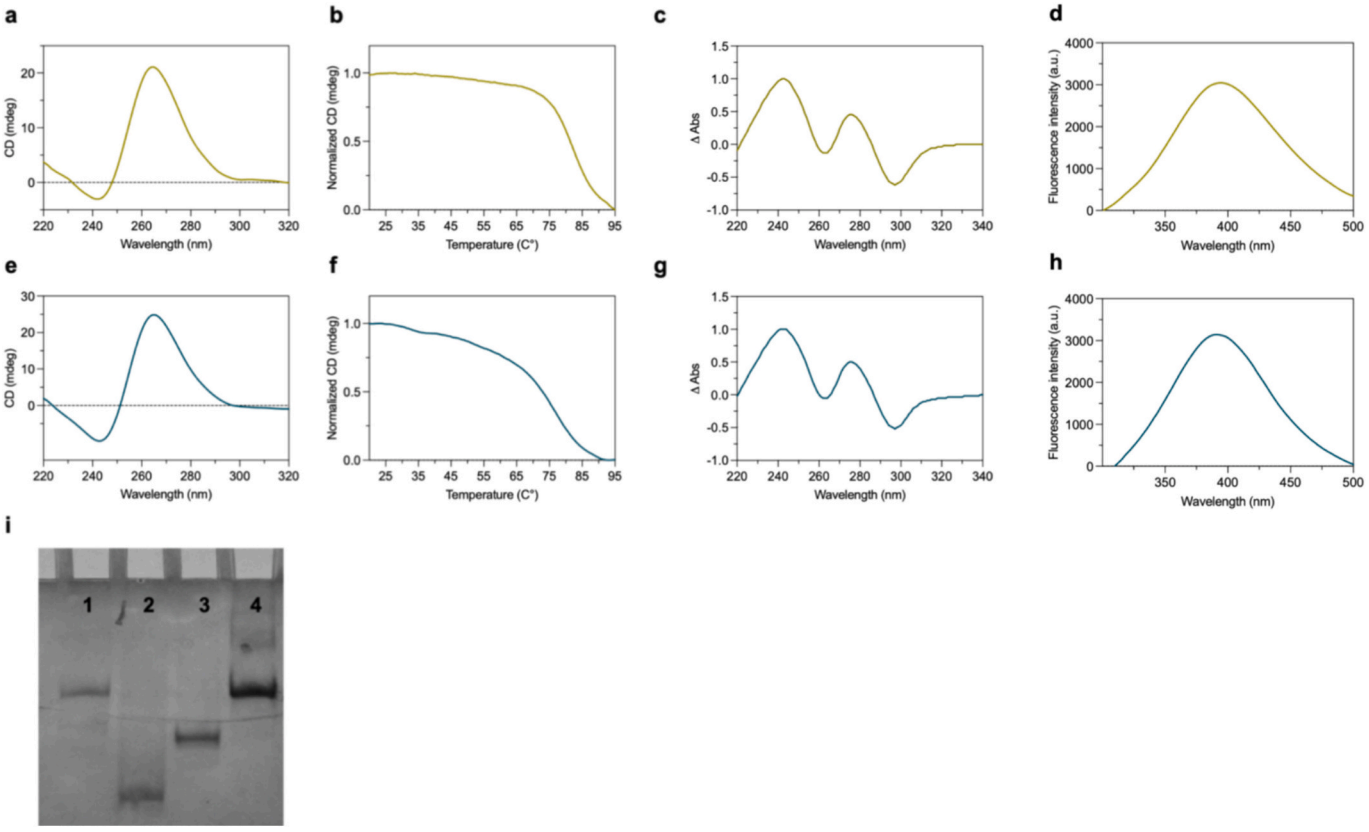

Fig. 6. CD spectra (a, e), CD melting curves (b, f), TDS profiles (c, g) and fluorescence (d, h) of STAT-U-FdU_{10} (a, b, c, d) and STAT-T-FdU_{10} (e, f, g, h), and their PAGE analysis (i) (lane 1: STAT-U-FdU_{10}; lane 2: STAT; lane 3: STAT-FdU_{10}; lane 4: STAT-T-FdU_{10}).

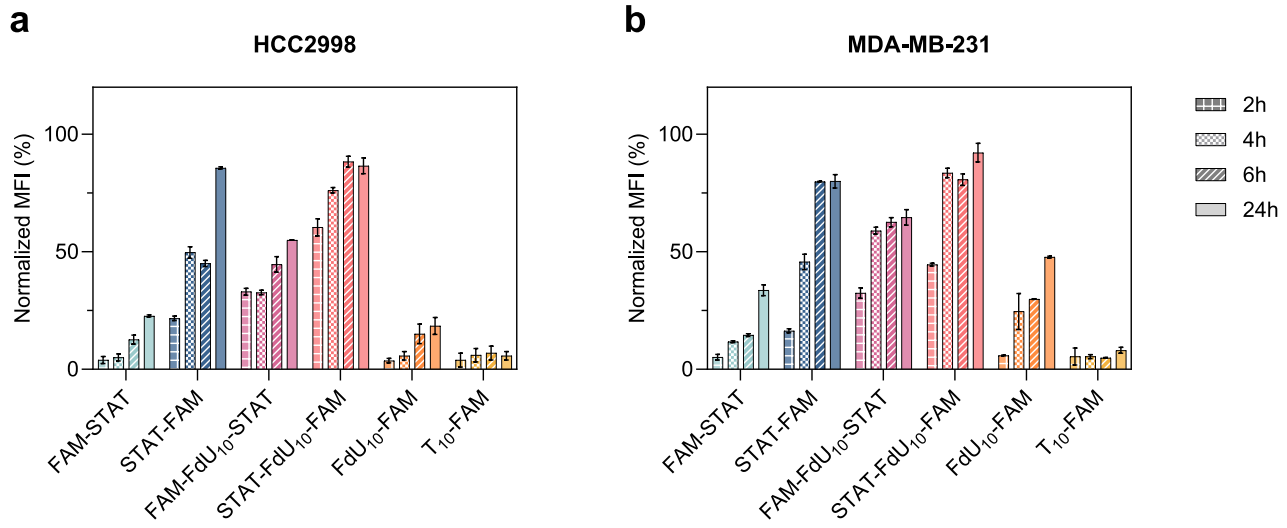

Fig. 7. Cellular internalization of FAM-labeled constructs at 2, 4, 6, and 24 h in HCC2998 (a), and MDA-MB-231 (b) cell lines. MFI: mean fluorescence intensity. See Table S2 for statistical analysis.

Finally, to assess cell type specificity, we evaluated internalization in PCS-201-012, a non-tumoral fibroblast line (Fig. S6). Results revealed almost no differences in uptake across compounds, with FdU_{10} alone showing the highest internalization, likely via gymnosis being favored by the fluorinated residues [10,26].

We next investigated the endocytic uptake mechanisms of STAT-FdU_{10} using a panel of inhibitors targeting distinct endocytic pathways. Flow cytometry analysis (Fig. S8) suggests that the dimeric species are internalized predominantly via a clathrin-mediated pathway. This uptake mechanism is consistent with the enhanced cellular internalization and uptake kinetics observed for these constructs in both cancer cell lines.

We further investigated the cellular localization of STAT-FdU_{10}-FAM (the lead construct in terms of cellular uptake) in MDA-MB-231 cells using confocal microscopy. Confocal microscopy analysis of MDA-MB-231 cells revealed that STAT-FdU_{10}-FAM was efficiently internalized and localized predominantly in the cytoplasm (Fig. S9). This highlights the ability of these constructs to efficiently enter tumor cells, an essential

prerequisite for subsequent biological activity.

3.3. Intracellular retention

Once internalized, aptamers must persist long enough to exert their biological effects and allow the intracellular release of drug payloads. To evaluate intracellular retention [52], we measured the intracellular signal at various time points following exposure to G4 constructs over 24 h period (Fig. 8 and Table S3). Cells were incubated with different constructs as in previous cellular uptake experiments. After 24 h of incubation, cells were washed to remove leftover material and then incubated in fresh media to be able to monitor either retained or excreted internalized structures. Following an additional 24 h (48 h from incubation with compounds) and 48 h (72 h from incubation) period, cells were washed, harvested, and analyzed by flow cytometry. The amount of retained material, normalized to the uptake at the initial 24-h time point, showed a decrease for all tested samples.

In HCC2998 cells, retention decreased to approximately 30% after 48 h and to 25–20% after 72 h of exposure. In contrast, MDA-MB-231 cells exhibited retention values ranging from 75% to 15% at 24 h and from 30% to 15% at 48 h. These findings are consistent with the majority of DNA residing in endosomal compartments capable of exocytosis. Notably, the 3′ end STAT-FdU_{10} dimer showed significantly longer intracellular retention than the monomeric 5′ end FdU_{10}-STAT in MDA-MB-231 cells after 24 h (48 h from incubation). This increased retention is likely resulting from several contributing factors. Enhanced uptake may result in larger intracellular pools, inherently increasing retention. These results suggest that the dimeric architecture supports longer intracellular residence times, thereby extending therapeutic exposure to the target site. In HCC2998 cells, there were slight differences in retention between compounds. Nevertheless, the 3′ end STAT-FdU_{10} maintained stable intracellular levels for up to 48 h, highlighting that the positional placement of the FdU tail contributes to sustained retention across different tumor models, slightly slowing down the transport of the constructs out of cells.

3.4. Cytotoxicity and synergistic antitumor activity

To further investigate whether prolonged intracellular persistence correlates with functional activity, we next assessed DNA damage responses and apoptotic markers, comparing the effects of dimeric and monomeric constructs in both cancer cell lines starting from 48 and 72 h of exposure.

MTT viability assays (Figs. 9, S10, Tables S4 and S5) revealed that the 3′-end FdU dimeric aptamer induced significantly higher cytotoxicity in cancer cells compared to both the 5′-end FdU_{10}-STAT monomer and the unmodified aptamer (STAT). Despite having identical FdU content as the monomeric species, the dimer exhibited superior efficacy across all tested concentrations. The difference between the monomer and the dimer is consistent with the internalization results, in which the dimer demonstrates enhanced cellular uptake and, consequently, a greater cytotoxic activity observed relative to the monomeric construct. The higher cytotoxicity for the dimer containing the FdU_{10} tail compared with STAT could be attributed to a synergistic action of the two functional domains of the construct. STAT inhibits the STAT3 pathway, associated with increased proliferation, immune evasion, and resistance to apoptosis [53]. Simultaneously, intracellular FdU is converted into FdUMP, which inhibits thymidylate synthase and disrupts DNA synthesis. The combination of pathway inhibition and DNA damage stress results in a significantly stronger antiproliferative response than either component alone, while maintaining the construct's targeting capability.

We further tested the compounds in fibroblast cells (non-tumor cell line) (Figs. 10, S11, and Table S4) to study whether the effect was different due to affinity to some cell-exposed factors. In this case, the levels of cell death caused by FdU_{10} alone were maintained; however, the dimeric form of STAT-FdU_{10} was much less cytotoxic than in both tumor cell lines, with more than 80% of cellular viability. This data suggests that the G4 aptamer serves as a targeting moiety of cancer cells, probably by means of nucleolin and/or STAT3-related receptors.

In both cancer cell lines, we observed increased toxicity at 72 h compared to the levels at 48 h. Although cytotoxicity in MDA-MB-231 cells was less pronounced at 48 h, by 72 h, STAT-FdU_{10} exhibited a cytotoxic effect comparable to that of FdU_{10}, reaching levels similar to those observed in HCC2998 cells. This effect could be attributed to the significantly longer intracellular retention of the 3′ end STAT-FdU_{10} dimer in MDA-MB-231 cells.

Finally, cell viability was further evaluated after 96 h of exposure. In both cancer cell lines, STAT-FdU_{10} exhibited greater cytotoxicity than FdU_{10}. We hypothesize that this effect is due to the slower degradation kinetics of the FdU_{10} tail, suggesting that the FdU_{10} moiety of the aptamer-drug chimera requires this extended incubation period of 96 h to reach higher cytotoxic activity [10]. In contrast, the cytotoxicity of STAT alone remained unchanged between 72 and 96 h, whereas STAT-FdU_{10} required prolonged exposure to reach high cytotoxicity. In fibroblasts, the additional 24 h underscored our hypothesis on the interaction of STAT with receptors selectively overexpressed in cancer cells, as evidenced by the strong reduction in cell viability of FdU_{10} and the

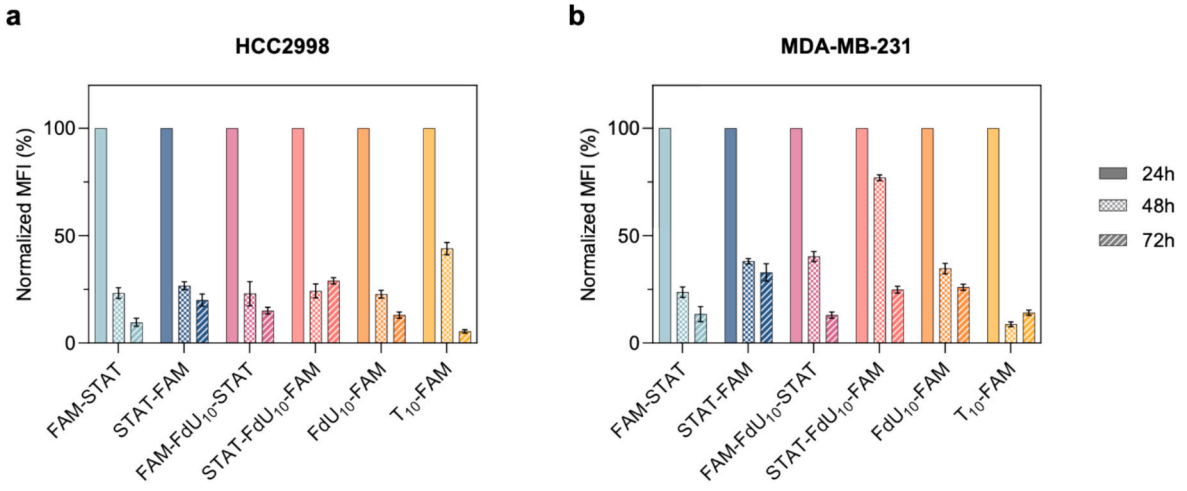

Fig. 8. Intracellular retention of FAM-labeled constructs at 1uM in HCC2998 (a), and MDA-MB-231 (b) cell lines. MFI: mean fluorescence intensity. See Table S3 for statistical analysis.

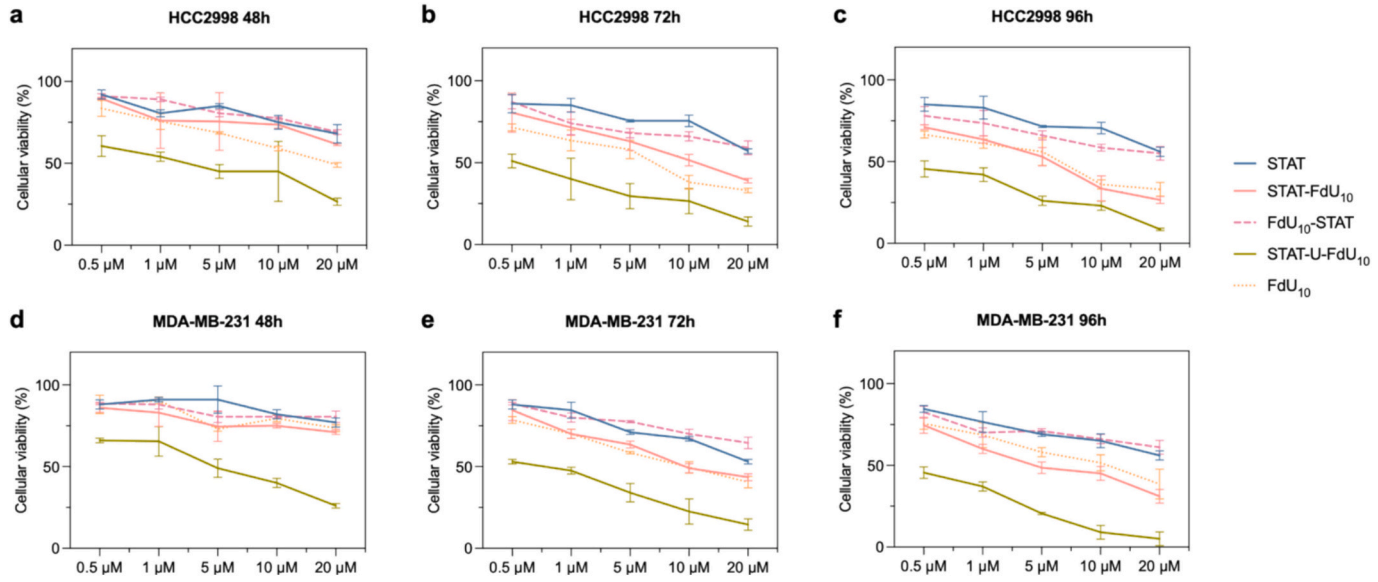

Fig. 9. MTT assay showing dose-dependent cytotoxicity of aptamer constructs. HCC2998 cells after 48 h (a), 72 h (b), and 96 h (c). MDA-MB-231 cells after (d) 48 h, (e) 72 h, and (f) 96 h. See Supporting Fig. S10 for controls and Supporting Table S4 statistical analysis.

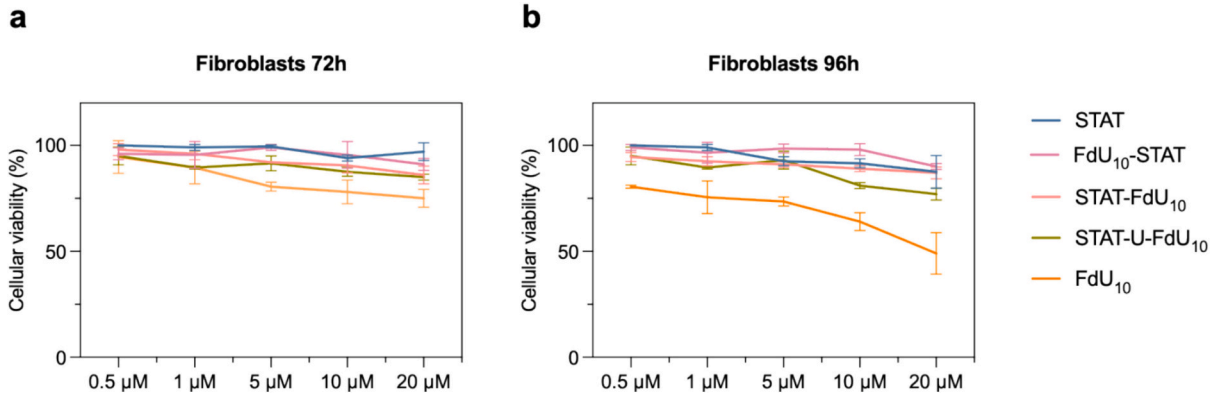

Fig. 10. MTT assay showing dose-dependent cytotoxicity of aptamer constructs in Fibroblasts after 72 h (a) and 96 h (b) of treatment. See Supporting Fig. S11 for controls and Supporting Table S4 for statistical analysis.

minimal cytotoxicity of STAT and STAT-FdU_{10}. Despite its significantly lower cellular uptake, FdU_{10} displayed cytotoxic activity comparable to that of the aptamer-drug conjugate, reflecting differences in cellular internalization and intracellular processing. FdU_{10} enters cells via gymnosis [26] and is rapidly degraded, enabling prompt generation of active metabolites that inhibit thymidylate synthase. In contrast, aptamer-drug conjugates are mainly internalized through clathrin-mediated endocytosis and require intracellular degradation to release the active FdU moiety. Importantly, although STAT-FdU_{10} and FdU_{10} display similar antiproliferative efficacy in cancer cells, FdU_{10} induces marked toxicity in non-malignant cells, whereas aptamer-drug conjugates show minimal off-target effects, highlighting the advantage of aptamer-based delivery strategies in improving cellular selectivity rather than merely increasing cytotoxic potency.

At this point, we sought to further enhance cytotoxicity at earlier times. We hypothesized that the insertion of a short RNA linker between the G4 sequence and the FdU_{10} tail would accelerate degradation and therefore promote faster prodrug activation [54]. The rationale behind this design was that the presence of a short RNA spacer could make the construct more vulnerable to RNases, which are more abundant and generally more efficient than DNases under physiological conditions. These spacers are intended to increase accessibility and, then, facilitate the nuclease action, thereby enhancing RNase-mediated cleavage.

Interestingly, the experimental results confirmed our hypothesis; in both tumor cell lines tested (Figs. 9, S10 and Table S4), the construct carrying the RNA linker exhibited an increase in cytotoxicity as early as 48 h after treatment, in contrast to the parental construct lacking the RNA insertion and the construct with a DNA linker (STAT-T-FdU_{10}). By 72 h, cellular viability had decreased approximately 35% even at the lowest concentration tested, highlighting the efficiency of the design. This data strongly suggests that the incorporation of a short RNA spacer accelerates degradation of the FdU_{10} tail, resulting in rapid activation of the prodrug moieties. Moreover, the greater inherent lability of RNA compared to DNA, combined with the high abundance of cellular RNases, contributes to the enhanced cytotoxic response. Overall, these findings support the conclusion that strategic incorporation of an RNA linker is an effective approach to accelerate prodrug activation and increase therapeutic potency at shorter exposure times.

To further characterize the mechanism of cell death, we performed apoptosis assays using Annexin V/PI staining after 72 h of treatment with 1 μM of each aptamer construct (Fig. 11 and Table S6) in both cancer cell lines. The 3′ end STAT-FdU_{10} dimer induced a significantly higher percentage of apoptotic cells compared to both the monomeric and unmodified constructs, with cells distributed across early and late

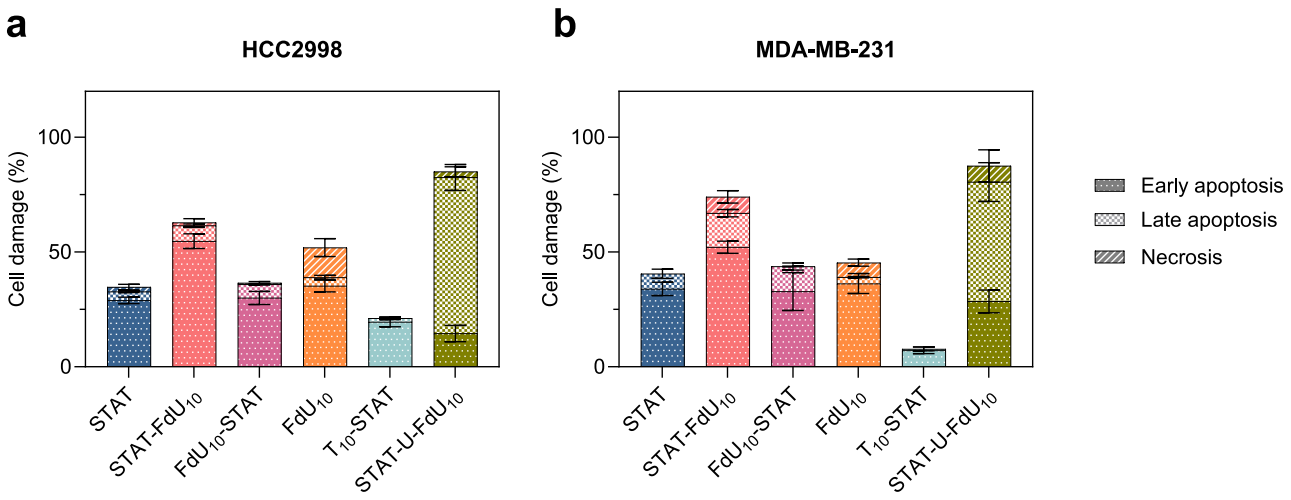

Fig. 11. Apoptosis studies. Annexin V/PI staining of cells treated with 1 μM STAT constructs in (a) HCC2998, and (b) MDA-MB-231 cells after 72 h of treatment. See Supporting Table S6 for statistical analysis.

apoptosis stages. Minimal necrosis was observed, indicating a specific and regulated cell death process rather than non-specific toxicity. Notably, the STAT-U-FdU_{10} construct exhibited a distinct shift, with a significantly higher number of cells in late apoptosis compared to STAT-FdU_{10}. These findings suggest that incorporation of the RNA spacer enhances the transition from early to late apoptosis. This shift highlights the critical role of the RNA spacer in accelerating degradation of the FdU_{10} tail and consequently potentiating cytotoxicity.

These results demonstrate that the dimeric aptamer construct effectively promotes apoptosis and a shift toward late apoptotic cell populations compared to FdU_{10}, through a combination of FdU-mediated DNA damage and STAT3 inhibition, reinforcing the notion of

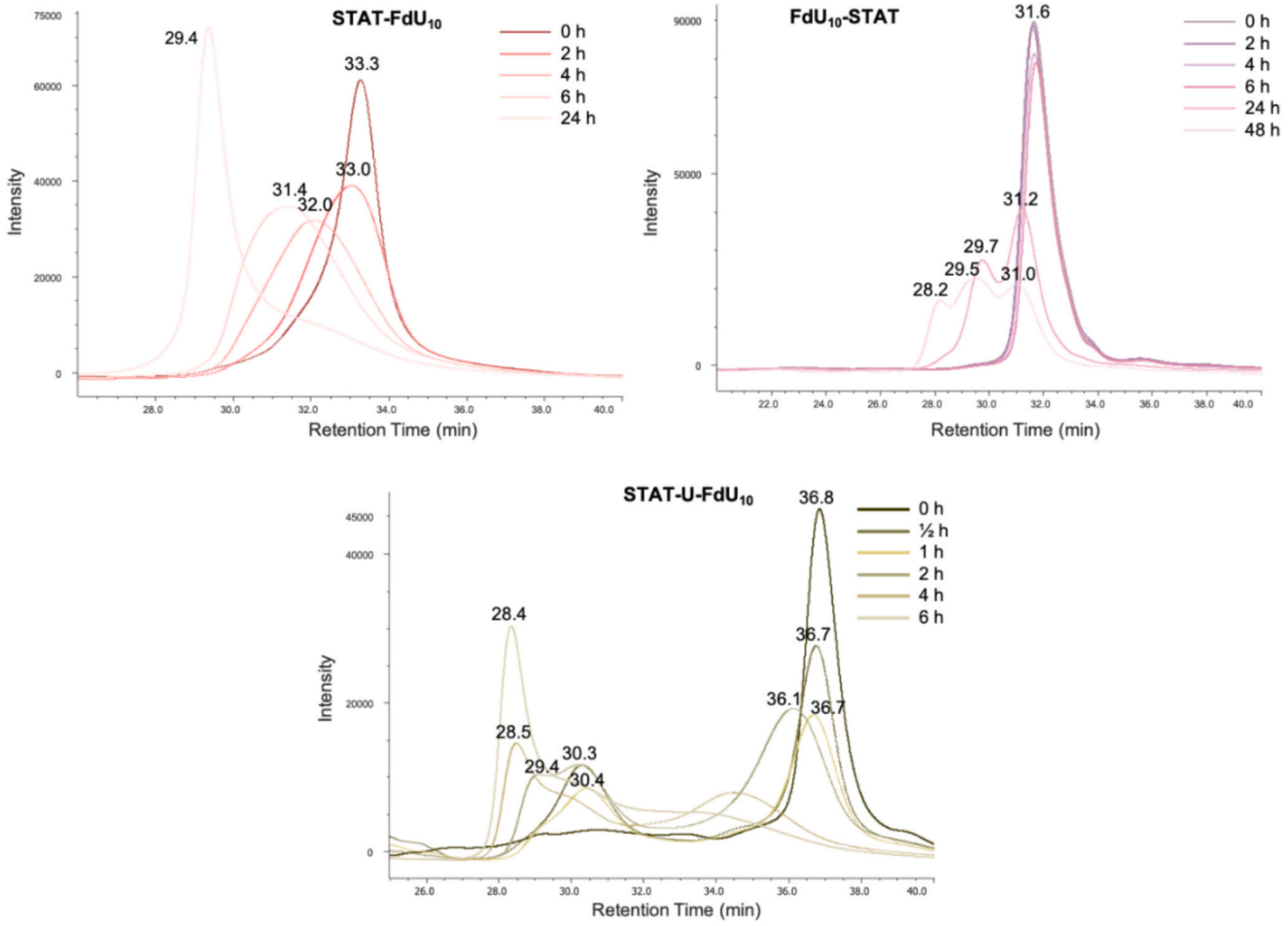

Fig. 12. Stability of the G4 derivatives in 10% FBS monitored by HPLC at different time points. The chromatogram region is expanded to highlight the degradation profile (for the complete chromatogram, see Supporting Fig. 12).

synergistic action. Moreover, this aligns with the retention and cytotoxicity data, supporting a model in which the dimer achieves superior delivery of active FdU metabolites to intracellular targets, it is retained longer and consequently the cytotoxic effect happens gradually. Between cell lines, MDA-MB-231 appears to be more sensitive to STAT-FdU_{10}, exhibiting a higher percentage of cells in the late apoptosis stage. In conclusion, the aptamer's STAT3-targeting action enhances apoptosis induction through thymidylate synthase inhibition, which likely weakens the tumor cell resistance to apoptotic stimuli, with a higher effect in the STAT-FdU_{10} dimeric form.

3.5. Nuclease stability assay

After assessing the different cytotoxic activities, we next investigated the serum stability of the conjugates and the ability of the aptamer scaffold to effectively release the FdU tail. STAT, the three FdU-bearing constructs, and the FdU_{10} tail alone were incubated in 10% FBS, and their degradation profiles were monitored by HPLC (Figs. 12, S12).

The chromatographic analysis reveals distinct release behaviors depending on the FdU tail nature and position.

The dimeric STAT-FdU_{10} conjugate exhibited a controlled and progressive cleavage of the FdU tail: within the first 6 h, a clear reduction in the main peak area was accompanied by a marked shift in retention time, while a concomitant increase in the early-eluting peak corresponding to free FdU confirmed the gradual detachment of the drug moiety. By 24 h, the chromatogram was largely dominated by the aptamer core, indicating that most of the cytotoxic moieties had been successfully detached and were free to exert their antiproliferative effect.

In sharp contrast, the monomeric construct bearing the FdU tail at the 5′ terminus (FdU_{10}-STAT) displayed markedly higher stability, maintaining both peak area and retention time throughout 6 h of incubation. Only after prolonged incubation (after 24 h and 48 h), a partial release of the FdU tail was detected, suggesting a delayed activation process. This behavior is fully consistent with the enhanced antiproliferative activity of the dimeric construct, suggesting that its partial susceptibility to serum degradation is functionally beneficial, as it enables controlled prodrug activation, unlike the monomeric construct, which shows only modest antiproliferative effects. The marked difference between the two architectures can be rationalized by the preferential action of more abundant 3′ exonucleases present in serum, which efficiently process the dimeric system while sparing the 5′-modified monomer.

A distinct profile was observed for the STAT-U-FdU hybrid, in which the presence of an RNA spacer between the aptamer and the drug introduced a preferential cleavage site, leading to a faster degradation with substantial release of the FdU tail already within the first 2 h. To further substantiate these findings and directly visualize the degradation pathway, the same serum stability assay was performed under identical experimental conditions and time points and subsequently analyzed by native PAGE (Fig. 13). In parallel, the structurally analogous construct incorporating a fully DNA-based linker, STAT-T-FdU_{10}, was evaluated under the same conditions in order to isolate the effect of linker chemistry on conjugate stability. PAGE analysis revealed an unambiguous difference between the two systems. STAT-T-FdU_{10} displayed a high stability, with the intact conjugate remaining predominant even at the longest incubation times, indicating strong resistance to nuclease throughout the assay. In contrast, STAT-U-FdU_{10} underwent a rapid and stepwise degradation process, characterized by the progressive appearance of multiple faster-migrating bands, which are indicative of successive cleavage events within the RNA-containing linker region. These intermediate species gradually evolve toward the predominant formation of the STAT core devoid of the FdU tail, clearly demonstrating efficient and controlled detachment of the drug moiety. Overall, these results highlight that linker composition represents a powerful design parameter to modulate degradation kinetics and enhance prodrug activation.

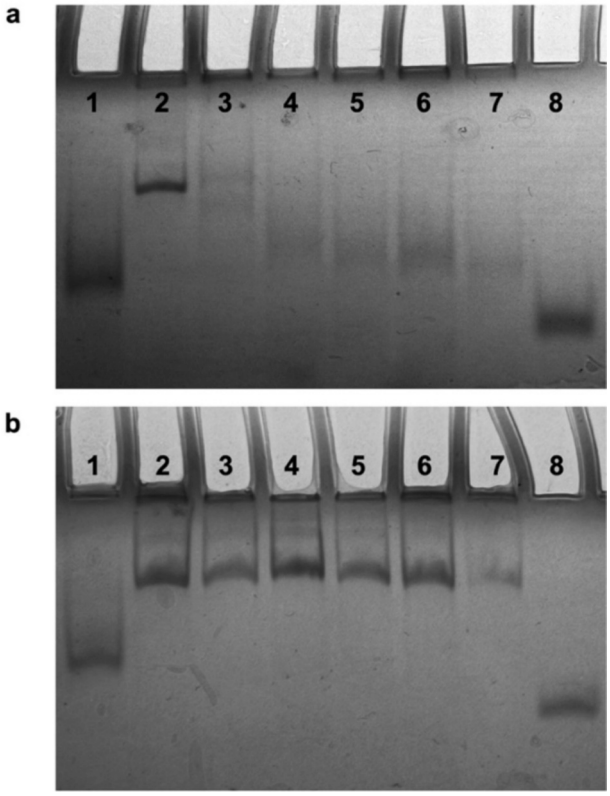

Fig. 13. Stability of STAT-U-FdU_{10} (a) and STAT-T-FdU_{10} (b) derivatives in 10% FBS, monitored by native PAGE. Lane 1: STAT aptamer; lane 2: STAT-U-FdU_{10} (a) or STAT-T-FdU_{10} (b) at T0; lanes 3–7: samples incubated for 30 min, 1 h, 2 h, 4 h, and 6 h, respectively; lane 8: T_{10} control oligonucleotide.

Importantly, in all cases, the STAT aptamer core remained intact following tail cleavage, thus confirming that even after drug release, the scaffold persists in its active form and can continue exerting its biological function (Fig. S12). Overall, these results clearly demonstrate that both the position and chemical nature of the FdU tail are decisive determinants of its release efficiency and, consequently, of the therapeutic outcome.

4. Conclusions

Our study demonstrates that the positional attachment of a 10-mer FdU tail to a G4-forming aptamer significantly influences its structural conformation and therapeutic efficacy. Structural investigations revealed that positioning the FdU sequence at the 3′ terminus preserves the formation of a dimeric G4 architecture, fully consistent with the intrinsic propensity of the unmodified STAT aptamer to form a 5′-5′ stacked dimer. In contrast, the analogous 5′-modified construct predominantly maintains a monomeric organization, as the presence of the tail at the 5′ end disrupts the dimer-favoring stacking interface.

These structural differences provide a solid mechanistic explanation for the observed divergence in biological performance. Notably, STAT-FdU_{10} results in a construct with significantly enhanced performance across multiple biological parameters, including cellular uptake, retention, cytotoxicity, and apoptosis induction, compared to its monomeric counterpart. The superior activity of the dimeric aptamer is likely due to multivalent binding effects, where two aptamer domains engage receptors more efficiently, increasing avidity and promoting more robust internalization. Prolonged intracellular retention may further support more effective delivery of the chemotherapeutic payload. Overall, the therapeutic performance of STAT-based FdU aptamers relies on a fine

balance between structural organization and controlled degradation of the drug-releasing tail. Crucially, the improved biological performance may also derive from faster and more efficient release of the FdU tail, and consequently of the drug, promoted by exonuclease processing, which ensures prompt intracellular activation of the cytotoxic component.

Building on this principle, the introduction of a short RNA spacer further validated the importance of degradation-driven activation. The presence of the RNA linker significantly increased nuclease accessibility and promoted rapid RNase-mediated processing of the FdU chain, thereby enabling earlier and more potent cytotoxic effects compared to the parental construct, underscoring the impact of spacer engineering on therapeutic performance.

Importantly, this construct is not merely a carrier-cargo combination but rather exhibits a synergistic therapeutic effect. The aptamer itself is specifically designed to bind and interfere with the STAT3 signaling pathway, a well-known driver of tumor progression and immune evasion. By engaging in this pathway, the aptamer contributes to tumor growth inhibition independently of the FdU tail. Simultaneously, FdU_{10} component (the thymidine analogues inhibit thymidylate synthase upon metabolic activation) further enhances DNA damage and apoptosis. The result is a dual mechanism of action, where the inhibition of both STAT3 signaling pathway and thymidylate synthase act cooperatively, enhancing overall cytotoxicity beyond the sum of their individual effects.

Furthermore, aptamer-mediated delivery offers therapeutic advantages over free FdU_{10}, which lacks targeting specificity and is associated with systemic toxicity and off-target effects. By directing FdU_{10} specifically to tumor cells through aptamer targeting, our strategy delivers the drug at tumor cells, potentially resulting in a reduction in side effects.

Overall, these findings highlight a powerful structure-function relationship in nucleic acid therapeutics, where precise positional control over a chemotherapeutic tail not only tunes molecular conformation but also enhances biological outcomes. The concept of combining a targeted nucleic acid scaffold (with therapeutic effect by itself and targeting capabilities) with a cytotoxic payload offers a synergistic and selective approach to cancer therapy. Furthermore, the incorporation of an RNA spacer emerges as a particularly promising avenue for optimizing aptamer-drug conjugates, enhancing degradation-driven activation and therapeutic performance.

Future directions include validating this synergistic effect in vivo, exploring pharmacokinetics and biodistribution, and expanding the approach to additional aptamer targets and drug types. Our results underscore the utility of conformation-guided, modular design in nucleic acid therapeutics and open new avenues for rationally engineered of next-generation aptamer-based cancer therapies.

CRediT authorship contribution statement

Natalia Navarro: Writing – review & editing, Writing – original draft, Validation, Methodology, Investigation, Formal analysis, Data curation, Conceptualization. **Daniela Benigno:** Writing – review & editing, Writing – original draft, Visualization, Validation, Methodology, Investigation, Formal analysis, Data curation, Conceptualization. **Carla Aliberti:** Investigation, Formal analysis, Data curation. **Antonella Virgilio:** Writing – review & editing, Supervision, Funding acquisition, Conceptualization. **Aldo Galeone:** Writing – review & editing, Supervision, Funding acquisition, Conceptualization. **Ramon Eritja:** Writing – review & editing, Supervision, Funding acquisition, Conceptualization. **Veronica Esposito:** Writing – review & editing, Supervision, Funding acquisition, Conceptualization. **Carme Fàbrega:** Writing – review & editing, Supervision, Funding acquisition, Conceptualization.

Funding

This work was supported by Spanish Ministerio de Ciencia e Innovación (MICINN) (Project PID2020-118145RB-I00 and PID2023-148655OB-I00) and by the European Union-NextGenerationEU-PNRR MUR-PRIN 2022-[CUP UNINA: E53D23009940006]. N.N. held a predoctoral contract grant (PRE2021-097856), CIBER-BBN is an initiative funded by the VI National R + D + I Plan 2008–2011, Iniciativa Ingenio 2010, Consolider Program, CIBER Actions and financed by the Instituto de Salud Carlos III with assistance from the European Regional Development. D.B. holds a research contract (art. 22 L. 240/2010 CUP: E63C25000640004) under the framework of the Piano Nazionale di Ripresa e Resilienza (PNRR)-Avviso MUR D.D. n. 47 del 20/02/2025 - Missione 4-Componente 2-Investimento 1.2 “Finanziamento di progetti presentati da giovani ricercatori”.

Declaration of competing interest

No conflict of interest.

Acknowledgements

We thank ICTS NANBIOSIS Oligonucleotide synthesis platform (U29). We thank the Biomolecular Analysis Unit (Mass Spectrometry for Molecular Characterization) of the Scientific and Technological Centers (CCiTUB), University of Barcelona.

Appendix A. Supplementary data

Supplementary data to this article can be found online at https://doi.org/10.1016/j.ijbiomac.2026.151523.

Data availability

Data will be made available on request.

References

[1] C. Roxo, W. Kotkowiak, A. Pasternak, G-quadruplex-forming aptamers—characteristics, applications, and perspectives, Molecules 24 (2019) 3781, https://doi.org/10.3390/molecules24203781.
[2] C. Platella, C. Riccardi, D. Montesarchio, G.N. Roviello, D. Musumeci, G-quadruplex-based aptamers against protein targets in therapy and diagnostics, Biochim. Biophys. Acta Gen. Subj. 2017 (1861) 1429–1447, https://doi.org/10.1016/j.bbagen.2016.11.027.
[3] K.R. Kampen, Membrane proteins: the key players of a cancer cell, J. Membr. Biol. 242 (2011) 69–74, https://doi.org/10.1007/s00232-011-9381-7.
[4] K. Prakash, S. Satishkartik, S. Ramalingam, P. Gangadaran, S. Gnanavel, K. N. Aruljothi, Investigating the multifaceted role of nucleolin in cellular function and cancer: structure, regulation, and therapeutic implications, Gene 957 (2025) 149479, https://doi.org/10.1016/j.gene.2025.149479.
[5] C. Roxo, W. Kotkowiak, A. Pasternak, G4 matters—the influence of G-quadruplex structural elements on the antiproliferative properties of G-rich oligonucleotides, Int. J. Mol. Sci. 22 (2021) 4941, https://doi.org/10.3390/ijms22094941.
[6] A.M. Zahedi, M. Pirouzbakht, S. Zanganeh, A. Afgar, Aptamer-drug conjugates (ApDCs): transformative approaches in targeted cancer therapy and precision oncology, Int. J. Pharm. 681 (2025) 125902, https://doi.org/10.1016/j.ijpharm.2025.125902.
[7] J.E. Rosenberg, R.M. Bambury, E.M. Van Allen, H.A. Drabkin, P.N. Lara, A. L. Harzstark, N. Wagle, R.A. Figlin, G.W. Smith, L.A. Garraway, T. Choueiri, F. Erlandsson, D.A. Laber, A phase II trial of AS1411 (a novel nucleolin-targeted DNA aptamer) in metastatic renal cell carcinoma, Investig. New Drugs 32 (2014) 178–187, https://doi.org/10.1007/s10637-013-0045-6.
[8] A. Van den Avont, N. Sharma-Walia, Anti-nucleolin aptamer AS1411: an advancing therapeutic, Front. Mol. Biosci. 10 (2023), https://doi.org/10.3389/fmolb.2023.1217769.
[9] W. Kotkowiak, N. Bartyś, A. Pasternak, Towards improved anticancer properties of the G-quadruplex-forming T40231 aptamer through increased flexibility of nucleoside residues, Sci. Rep. 15 (2025) 25159, https://doi.org/10.1038/s41598-025-09934-8.
[10] D. Benigno, N. Navarro, A. Aviñó, V. Esposito, A. Galeone, A. Virgilio, C. Fàbrega, R. Eritja, Aptamer-drug conjugates for a targeted and synergistic anticancer response: exploiting T30923-5-fluoro-2′-deoxyuridine (INT-FdU) derivatives, Eur. J. Pharm. Biopharm. 201 (2024), https://doi.org/10.1016/j.ejpb.2024.114354.
[11] A.M. Ogloblina, A.N. Khristich, N.Y. Karpechenko, S.E. Semina, G.A. Belitsky, N. G. Dolinnaya, M.G. Yakubovskaya, Multi-targeted effects of G4-aptamers and their antiproliferative activity against cancer cells, Biochimie 145 (2018) 163–173, https://doi.org/10.1016/j.biochi.2017.11.020.

[12] A. Virgilio, A. Pecoraro, D. Benigno, A. Russo, G. Russo, V. Esposito, A. Galeone, Antiproliferative effects of the aptamer d(GGGT)4 and its analogues with an abasic-site mimic loop on different cancer cells, Int. J. Mol. Sci. 23 (2022), https://doi.org/10.3390/ijms23115952.
[13] D. Benigno, A. Virgilio, I. Bello, S. La Manna, V. Vellecco, M. Bucci, D. Marasco, E. Panza, V. Esposito, A. Galeone, Properties and potential antiproliferative activity of thrombin-binding aptamer (TBA) derivatives with one or two additional G-tetrads, Int. J. Mol. Sci. 23 (2022), https://doi.org/10.3390/ijms232314921.
[14] Y. Li, T.N. Zamay, N.A. Luzan, E.A. Pryakhin, E.V. Styazhkina, L.A. Osminkina, O. S. Kolovskaya, M.A. Dymova, E.V. Kuligina, V.A. Richter, A.G. Bkhattachariia, D. A. Bydanov, A.V. Galantsev, I.A. Vostrov, Z. Liu, G.S. Zamay, A.S. Kichkailo, X.-Q. Wang, Aptamers as a new frontier in targeted cancer therapy, Adv. Drug Deliv. Rev. 226 (2025) 115692, https://doi.org/10.1016/j.addr.2025.115692.
[15] S. Ni, H. Yao, L. Wang, J. Lu, F. Jiang, A. Lu, G. Zhang, Chemical modifications of nucleic acid aptamers for therapeutic purposes, Int. J. Mol. Sci. 18 (2017) 1683, https://doi.org/10.3390/ijms18081683.
[16] F. Odeh, H. Nsairat, W. Alshaer, M.A. Ismail, E. Esawi, B. Qaqish, A. Al Bawab, S. I. Ismail, Aptamers chemistry: chemical modifications and conjugation strategies, Molecules 25 (2019) 3, https://doi.org/10.3390/molecules25010003.
[17] S. Ni, Z. Zhuo, Y. Pan, Y. Yu, F. Li, J. Liu, L. Wang, X. Wu, D. Li, Y. Wan, L. Zhang, Z. Yang, B.-T. Zhang, A. Lu, G. Zhang, Recent progress in aptamer discoveries and modifications for therapeutic applications, ACS Appl. Mater. Interfaces 13 (2021) 9500–9519, https://doi.org/10.1021/acsami.0c05750.
[18] R. Bavi, Z. Hang, P. Banerjee, M. Aquib, M. Jadhao, N. Rane, S. Bavi, R. Bhosale, K. Kodam, B.-H. Jeon, Y. Gu, Doxorubicin-conjugated innovative 16-mer DNA aptamer-based annexin A1 targeted anti-cancer drug delivery, Mol. Ther. Nucleic Acids 21 (2020) 1074–1086, https://doi.org/10.1016/j.omtn.2020.07.038.
[19] L. Tang, R. Tong, V.J. Coyle, Q. Yin, H. Pondenis, L.B. Borst, J. Cheng, T.M. Fan, Targeting tumor vasculature with aptamer-functionalized doxorubicin–polylactide nanoconjugates for enhanced cancer therapy, ACS Nano 9 (2015) 5072–5081, https://doi.org/10.1021/acsnano.5b00166.
[20] A. Clua, C. Fàbrega, J. García-Chica, S. Grijalvo, R. Eritja, Parallel G-quadruplex structures increase cellular uptake and cytotoxicity of 5-fluoro-2′-deoxyuridine oligomers in 5-fluorouracil resistant cells, Molecules 26 (2021), https://doi.org/10.3390/molecules26061741.
[21] A. Clua, C. Fàbrega, D. Musumeci, F. Doria, V. Pirota, F. Ghirga, C. Platella, R. Eritja, D. Montesarchio, On the interaction of anticancer G-quadruplex ligands with GalNAc-functionalized G-quadruplex-forming carriers for selective recognition and treatment of hepatocellular carcinoma, Bioorg. Chem. 157 (2025) 108299, https://doi.org/10.1016/j.bioorg.2025.108299.
[22] L. Zhu, J. Yang, Y. Ma, X. Zhu, C. Zhang, Aptamers entirely built from therapeutic nucleoside analogues for targeted cancer therapy, J. Am. Chem. Soc. 144 (2022) 1493–1497, https://doi.org/10.1021/jacs.1c09574.
[23] Z.-Y. Liao, O. Sordet, H.-L. Zhang, G. Kohlhagen, S. Antony, W.H. Gmeiner, Y. Pommier, A novel polypyrimidine antitumor agent FdUMP[10] induces thymineless death with topoisomerase I-DNA complexes, Cancer Res. 65 (2005) 4844–4851, https://doi.org/10.1158/0008-5472.CAN-04-1302.
[24] W.H. Gmeiner, W. Debinski, C. Milligan, D. Caudell, T.S. Pardee, The applications of the novel polymeric fluoropyrimidine F10 in cancer treatment: current evidence, Future Oncol. 12 (2016) 2009–2020, https://doi.org/10.2217/fon-2016-0091.
[25] A. Aviñó, A. Clua, M.J. Bleda, R. Eritja, C. Fàbrega, Evaluation of floxuridine oligonucleotide conjugates carrying potential enhancers of cellular uptake, Int. J. Mol. Sci. 22 (2021), https://doi.org/10.3390/ijms22115678.
[26] N. Navarro, S. Serantes, A. Aviñó, C. Fàbrega, R. Eritja, Synthesis and evaluation of 3′-oleyl–oligonucleotide conjugates as potential cellular uptake enhancers, Synlett (2023), https://doi.org/10.1055/s-0042-1751528.
[27] N. Navarro, A. Aviñó, Ò. Domènech, J.H. Borrell, R. Eritja, C. Fàbrega, Defined covalent attachment of three cancer drugs to DNA origami increases cytotoxicity at nanomolar concentration, Nanomedicine 55 (2024) 102722, https://doi.org/10.1016/j.nano.2023.102722.
[28] A.F. Jorge, A. Aviñó, A.A.C.C. Pais, R. Eritja, C. Fàbrega, DNA-based nanoscaffolds as vehicles for 5-fluoro-2′-deoxyuridine oligomers in colorectal cancer therapy, Nanoscale 10 (2018) 7238–7249, https://doi.org/10.1039/c7nr08442k.
[29] A. Ramos-Valle, A. Domínguez, N. Navarro, A. Márquez-López, A. Aviñó, R. Eritja, C. Fàbrega, L. García-Hevia, Mónica.L. Fanarraga, Targeted tumor microenvironment delivery of floxuridine prodrug via soluble silica nanoparticles in malignant melanoma as a model for aggressive cancer treatment, Small 21 (2025), https://doi.org/10.1002/smll.202407752.
[30] N.Q. Do, A.T. Phan, Monomer-dimer equilibrium for the 5′-5′ stacking of propeller-type parallel-stranded g-quadruplexes: NMR structural study, Chem. Eur. J. 18 (2012) 14752–14759, https://doi.org/10.1002/chem.201103295.
[31] R. Yazdian-Robati, P. Bayat, F. Oroojalian, M. Zargari, M. Ramezani, S.M. Taghdisi, K. Abnous, Therapeutic applications of AS1411 aptamer, an update review, Int. J. Biol. Macromol. 155 (2020) 1420–1431, https://doi.org/10.1016/j.ijbiomac.2019.11.118.
[32] M. Askarzadeh, M. Rajabinejad, A. Rafiei, M. Hashemi, R. Yazdian-Robati, AS1411 aptamer in melanoma therapy: harnessing targeted strategies for precision treatment, Pathol. Res. Pract. 273 (2025) 156124, https://doi.org/10.1016/j.prp.2025.156124.
[33] F. Li, J. Lu, J. Liu, C. Liang, M. Wang, L. Wang, D. Li, H. Yao, Q. Zhang, J. Wen, Z.-K. Zhang, J. Li, Q. Lv, X. He, B. Guo, D. Guan, Y. Yu, L. Dang, X. Wu, Y. Li, G. Chen, F. Jiang, S. Sun, B.-T. Zhang, A. Lu, G. Zhang, A water-soluble nucleolin aptamer-paclitaxel conjugate for tumor-specific targeting in ovarian cancer, Nat. Commun. 8 (2017) 1390, https://doi.org/10.1038/s41467-017-01565-6.
[34] B.T. Tran, J. Kim, D.-R. Ahn, Systemic delivery of aptamer–drug conjugates for cancer therapy using enzymatically generated self-assembled DNA nanoparticles, Nanoscale 12 (2020) 22945–22951, https://doi.org/10.1039/D0NR05652A.
[35] P. Lourenço, D. Moreira, A. Miranda, J. Lopes-Nunes, I. Maocha, T. Santos, P. L. Ferreira, F. Sousa, A. Paiva, C. Cruz, Exploring the G-quadruplex formation of AS1411 derivatives, Molecules 30 (2025) 1673, https://doi.org/10.3390/molecules30081673.
[36] P. Weerasinghe, G.E. Garcia, Q. Zhu, P. Yuan, L. Feng, L. Mao, N. Jing, Inhibition of Stat3 activation and tumor growth suppression of non-small cell lung cancer by G-quartet oligonucleotides, Int. J. Oncol. 31 (2007) 129–136.
[37] V. Esposito, D. Benigno, I. Bello, E. Panza, M. Bucci, A. Virgilio, A. Galeone, Structural and biological features of G-quadruplex aptamers as promising inhibitors of the STAT3 signaling pathway, Int. J. Mol. Sci. 24 (2023), https://doi.org/10.3390/ijms24119524.
[38] H. Yu, D. Pardoll, R. Jove, STATs in cancer inflammation and immunity: a leading role for STAT3, Nat. Rev. Cancer 9 (2009) 798–809, https://doi.org/10.1038/nrc2734.
[39] M. Tolomeo, A. Cascio, The multifaced role of STAT3 in cancer and its implication for anticancer therapy, Int. J. Mol. Sci. 22 (2021) 603, https://doi.org/10.3390/ijms22020603.
[40] Y. Hu, Z. Dong, K. Liu, Unraveling the complexity of STAT3 in cancer: molecular understanding and drug discovery, J. Exp. Clin. Cancer Res. 43 (2024) 23, https://doi.org/10.1186/s13046-024-02949-5.
[41] N.Q. Do, K.W. Lim, M.H. Teo, B. Heddi, A.T. Phan, Stacking of G-quadruplexes: NMR structure of a G-rich oligonucleotide with potential anti-HIV and anticancer activity, Nucleic Acids Res. 39 (2011) 9448–9457, https://doi.org/10.1093/nar/gkr539.
[42] V. Esposito, D. Benigno, C. Aliberti, C. Esposito, E. Panza, A. Virgilio, A. Galeone, Effects of 5-methyl-2′-deoxycytidine in G-quadruplex forming aptamers d(G3C)4 and d[GCG2(CG3)3C]: investigating the key role of the loops, Biomolecules 15 (2025) 753, https://doi.org/10.3390/biom15060753.
[43] A.P. Guzaev, Solid-phase supports for oligonucleotide synthesis, Curr. Protoc. Nucleic Acid Chem. 53 (2013), https://doi.org/10.1002/0471142700.nc0301s53.
[44] J.-L. Mergny, Thermal difference spectra: a specific signature for nucleic acid structures, Nucleic Acids Res. 33 (2005) e138, https://doi.org/10.1093/nar/gni134.
[45] N.T. Dao, R. Haselsberger, M. Michel-Beyerle, A.T. Phan, Excimer formation by stacking G-quadruplex blocks, ChemPhysChem 14 (2013) 2667–2671, https://doi.org/10.1002/cphc.201300481.
[46] S. Gao, Y. Cao, Y. Yan, X. Xiang, X. Guo, Correlations between fluorescence emission and base stacks of nucleic acid G-quadruplexes, RSC Adv. 6 (2016) 94531–94538, https://doi.org/10.1039/C6RA21347B.
[47] M. Zuffo, A. Gandolfini, B. Heddi, A. Granzhan, Harnessing intrinsic fluorescence for typing of secondary structures of DNA, Nucleic Acids Res. 48 (2020) e61, https://doi.org/10.1093/nar/gkaa257.
[48] A. Virgilio, D. Benigno, A. Pecoraro, A. Russo, G. Russo, V. Esposito, A. Galeone, Exploring new potential anticancer activities of the g-quadruplexes formed by [(GTG2T(G3T)3] and its derivatives with an abasic site replacing single thymidine, Int. J. Mol. Sci. 22 (2021), https://doi.org/10.3390/ijms22137040.
[49] Y. Du, Q. Wang, L. Shi, T. Li, G-quadruplex-proximized aptamers (G4PA) efficiently targeting cell-surface transferrin receptors for targeted cargo delivery, Nano Lett. 22 (2022) 6328–6333, https://doi.org/10.1021/acs.nanolett.2c02064.
[50] C. Liu, Q. Wang, L. Shi, T. Li, Robust G-quadruplex dimer-guided transmembrane DNA nanovehicles for targeted payload delivery, Anal. Sens. 5 (2025), https://doi.org/10.1002/anse.202400048.
[51] C. Riccardi, E. Napolitano, D. Musumeci, D. Montesarchio, Dimeric and multimeric DNA aptamers for highly effective protein recognition, Molecules 25 (2020) 5227, https://doi.org/10.3390/molecules25225227.
[52] T.M. Brown, D. Saliba, J. Hartmann, J. Asohan, C. Yao, T. Das, H.F. Sleiman, UV-cross-linked DNA nanomaterials enable robust nanopatterning of folate ligands for enhanced cellular uptake, J. Am. Chem. Soc. 147 (2025) 18876–18887, https://doi.org/10.1021/jacs.5c02986.
[53] E.Z.P. Chai, M.K. Shanmugam, F. Arfuso, A. Dharmarajan, C. Wang, A.P. Kumar, R. P. Samy, L.H.K. Lim, L. Wang, B.C. Goh, K.S. Ahn, K.M. Hui, G. Sethi, Targeting transcription factor STAT3 for cancer prevention and therapy, Pharmacol. Ther. 162 (2016) 86–97, https://doi.org/10.1016/j.pharmthera.2015.10.004.
[54] K.C. Aluri, D. Datta, S. Waldron, N. Taneja, J. Qin, D.P. Donnelly, C.S. Theile, D. C. Guenther, L. Lei, J.M. Harp, P.S. Pallan, M. Egli, I. Zlatev, M. Manoharan, Single-stranded hairpin loop RNAs (loopmeRNAs) potently induce gene silencing through the RNA interference pathway, J. Am. Chem. Soc. (2024), https://doi.org/10.1021/jacs.4c07902.